

Self-powered shape-transforming membranes: an active-matter approach to soft robotics

Ido Levin¹, Robert Deegan² and Eran Sharon^{1*}

¹*Racah Institute of Physics, The Hebrew University, Jerusalem 91904, Israel*

²*Department of Physics & Center for the Study of Complex Systems University of Michigan,
Ann Arbor, MI 48109, USA*

**correspondence to: erans@mail.huji.ac.il*

We present the first example of an autonomous, extended, shape-transforming sheet made from a gel that shrinks and swells in response to the Belousov-Zhabotinsky (BZ) reaction. BZ waves traveling within the gel induce periodic flapping of the sheets. We compute the relationship between the reference Gaussian curvature and the reaction phase using the theory of non-Euclidean elasticity and show that this quantitatively predicts the evolving three-dimensional shape. We account for deviations from the purely geometric theory due to finite-thickness effects. This system demonstrates behavior reminiscent of biological organisms: autonomous shape changes of a soft slender structure powered by chemical free energy extracted from the environment. Our results constitute an important step towards the realization of autonomous soft machines.

From an amoeba's ability to extend pseudopods to the fast active tissue deformations in multi-cellular primitive animals to the muscle contractions of higher animals, nature provides countless examples of soft materials undergoing autonomous mechanical deformations [1-3]. These have inspired the emerging field of soft robotics [4] with the aim of exploiting the flexibility of soft materials to create robots with novel capabilities. Early successes include self-powered walkers propelled by uniaxial deformations [5,6], pneumatically-actuated robots [7], externally-driven hybrids of natural and man-made materials [8] and combinations of soft materials with discrete actuators [9]. However, to-date the holy grail of soft robotics – an autonomous, reconfigurable, high-deformation platform – has yet to be developed. Here we present a major step towards this goal by showing that multi-axial deformations are achievable in a quasi-two-dimensional, self-powered, gel material. These planar deformations induce dynamic three-dimensional (3D) configurations that are predictable and quantitatively modeled by the theory of incompatible elastic sheets.

In recent years our understanding of the elasticity of thin sheets has advanced greatly with the discovery of computational tools, namely the theory of non-Euclidean plates (NEPs) and shells [10,11]. The theory shows that thin sheets adopt an *actual* geometry determined by the *reference* geometry as inputs for minimizing the elastic energy functional:

$$E[\mathbf{a}, \mathbf{b}] = \int d\bar{s} \left[h(\mathbf{a} - \bar{\mathbf{a}})^2 + h^3(\mathbf{b} - \bar{\mathbf{b}})^2 \right] \quad 1$$

where $\{\mathbf{a}, \bar{\mathbf{a}}\}$ are the metric tensors and $\{\mathbf{b}, \bar{\mathbf{b}}\}$ are the curvature tensors for the actual and the reference geometry, respectively, and h is the thickness of the sheet. Typically, the reference metric and curvature tensors are geometrically incompatible: no two-dimensional (2D) surface with this geometry can be formed in a 3D space. In this case, the elastic energy does not vanish and the actual geometry emerges from a competition between bending and stretching, the connection between the reference and actual geometries is highly non-trivial and symmetry breaking, multi-scale solutions and, refinement with thickness may occur, depending on the body dimensions and the prescribed geometry [12-18].

Prior work on thin sheets has yielded a variety of methods for manipulating the reference metric and curvature. Irreversible methods include plastic deformation [19] and inter-diffusing bi-materials [20]; reversible methods include responsive gels [15,18,21], nematic elastomers [22,23], inflatable meta-materials [24] and dielectric elastomers [25]. These results have established the validity of the incompatible elasticity framework and provided guidelines for shape selection. However, these methods do not include autonomy since their activation depends on an external field, such as temperature, salinity, or stress. Moreover, these methods are typically global, meaning that the control signal is spatially uniform. Local time-varying reference geometries [26] have been shown but this technique depends on external controls, too.

In summary, currently available methods for manipulating the geometry of soft materials are unsuitable for achieving autonomy. What is needed instead is an internal, spatially-varying actuation and control scheme. Such a scheme would make the most out of a soft system's capacity for large and complex deformation. A material with the potential to encompass these properties was developed by Yoshida and coworkers [27]. They covalently bonded the metal catalyst of the Belousov-Zhabotinsky (BZ) reaction to a thermal responsive gel of N-isopropylacrylamide (NIPA). NIPA by itself undergoes a hydrophilic to hydrophobic transition above a critical temperature, causing the gel to shrink by several hundred percent. The BZ reaction by itself produces oscillations of the metal catalyst between redox states. When incorporated into NIPA, the charge of the metal catalyst shifts the critical temperature of the hydrophobic-hydrophilic transition and the ratio between equilibrium volume in the two phases. By selecting the ambient temperature appropriately, oscillations between the redox states cause volume oscillations of the gel, or rather, in the language we shall use here, between different reference geometries. Moreover, since the BZ reaction can sustain pattern forming chemical waves, shaped as either spirals or targets, Yoshida's BZ-gels enable both autonomous and local control.

BZ-gels have been used to induce time-varying bending of beams [5], transport, and peristaltic pumping [28]. Motivated by these observations, multi-physics simulations of three-dimensional poro-elastic systems coupled to the Oregonator model of BZ reaction, revealed additional phenomena [29-31]. However, an analytically tractable *effective* theory, in the form of a coupled system of reaction-diffusion and non-Euclidean plate, has not yet been studied.

Here we report the first autonomous NEPs: extended thin sheets with a time-evolving geometry. We use a BZ-gel as the active material. Our NEPs spontaneously convert chemical energy extracted from the environment into mechanical work that manifests as periodic changes of their 3D shape. We find a deterministic empirical relation between the reaction field and the local equilibrium volume. Next, we show that the evolving shape is well-described by the theory of incompatible elastic sheets: the BZ reaction produces a time-dependent reference metric via a dynamical conformal transformation of the Euclidean metric. We determine the relationship between the dynamics of the chemical reaction and the evolution of the metric, and from it compute the induced reference Gaussian-curvature, an intrinsic geometrical quantity important for determining the 3D shape. Dynamic 3D measurements of the evolving sheets confirm the presence of propagating fronts of Gaussian-curvature, induced by the BZ reaction. Lastly, we measure and discuss the impact of various time and length scales on the evolving shape, including a time delay between the BZ phase and the induced swelling, and finite thickness effects, such as a curvature cutoff. The latter produce deviations of the actual shape from the reference geometry of the sheet, consistent with analytic studies [32] and finite element simulations.

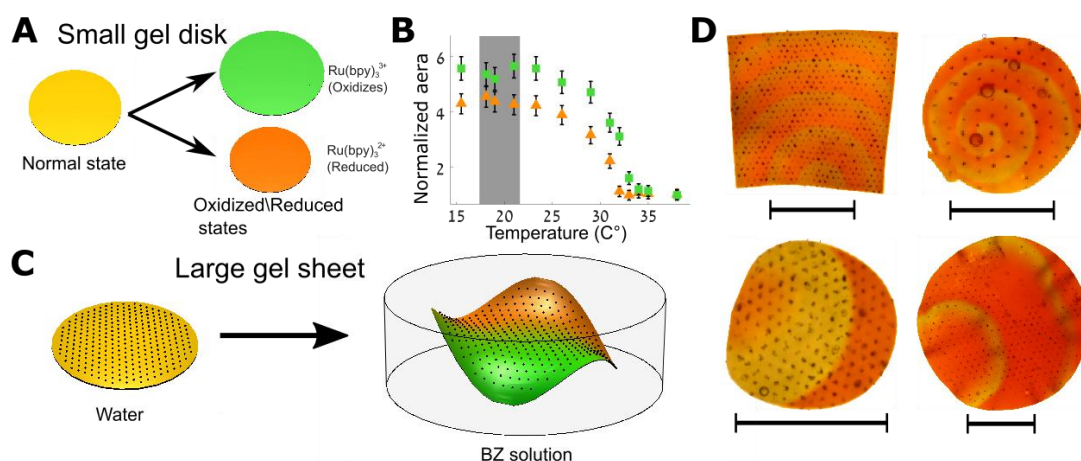


Fig. 1. Experimental apparatus: **(A)** The redox state of the ruthenium monomer determines the equilibrium volume of a BZ-gel disk. The area of our gels is typically 1.5 times larger in the oxidized state than in the reduced state. **(B)** The equilibrium area of the BZ-gel in the oxidized (green) and reduced (orange) states normalized by the oxidized area at 40 °C versus temperatures exhibits a sharp phase-transition around 30 °C. Experiments were performed at 20 °C (gray area), where temperature variations have negligible effect on the area in either state. **(C)** A BZ-gel in a solution of the BZ reactants develops green oxidation traveling-fronts that induce spatially inhomogeneous swelling and, as a result, global shape changes. **(D)** Different spatiotemporal patterns (phase, target, and spiral waves) emerge depending on the chemical concentrations and the geometry of the gel, leading to different mechanical responses (scale bar is 1cm long). Discs that are small compared to the wavelength buckle globally (bottom left), while larger ones respond to the reaction phase more locally and produce wrinkled structures (bottom right).

We prepared BZ-gel discs 0.5-5 cm in diameter by copolymerizing and crosslinking NIPA and ruthenium monomers according to [5] (see SI). When placed in a solution of the substrate BZ reactants (i.e. all the BZ reactant except the metal catalyst), waves of the redox state, visible in Fig. 1A,B as color changes, generate local variations of the equilibrium volume of the gel (Fig. 1A,B). Unlike small gel flakes that oscillate homogeneously [33], the phase of the reaction in our samples varies spatially and temporally [27]; these phase variations take the form of propagating fronts with either a target-like or spiral pattern depending on experimental conditions (Fig. 1D). The gradients in swelling produced by the chemical waves

induce local changes of the sheet's curvature that translate to periodic three-dimensional flapping on the global scale synchronized to the reaction (Fig. 2 and Movie S1).

We measure the 3D shape of the gel on a triangulated mesh at 5 second intervals using a home-built stereoscopy apparatus that images a grid of dots printed on the top surface of the gel (see SI, Fig 1C, Fig. S1 and Movie S3). Since the triangulation is Lagrangian, i.e. fixed to material points, we can extract local geometrical properties, such as swelling, height, reference metric and curvature. In addition, we obtain the phase, ϕ , of the BZ reaction field from the green channel of the images.

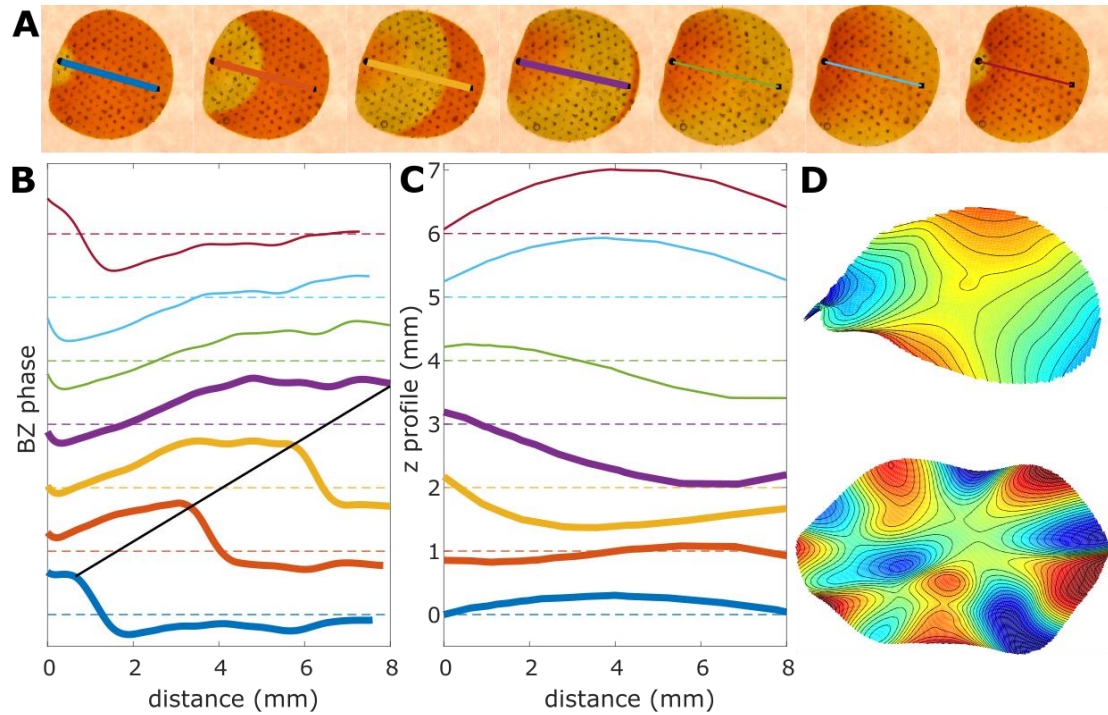


Fig. 2. BZ front and the resultant plate bending propagation as a function of position: **(A)** Time-lapse of a single wavelength of a BZ target-like waveform within a gel imaged at 80 seconds intervals. **(B)** The redox phase of the BZ-reaction for each image in (A) along the colored lines. The phase of the reaction is extracted from the green channel of the image along the marked line. The sharp leading front propagates (thick lines) with a speed of 30 $\mu\text{m/s}$ (see black line) followed by a relaxation toward the reduced state caused by the dispersed trailing front (thin lines). The dashed line corresponds to the zero phase for each curve. Colors in (B) correspond to line colors in (A). **(C)** The height profiles for each image in (A) along the color lines. The dashed lines are the plane of zero elevation for the corresponding curve. These data show significant curvature changes, including a change of sign (compare yellow and teal lines), and a global geometric response even though the BZ-phase variation is greatest at the front. **(D)** Three-dimensional configurations of two gel sheets, showing typical elastic solutions: Global-type solution (top), where the entire sheet buckles out-of-plane and a wrinkled-type solution (bottom panels) displaying an emergent length-scale. Both configurations are due to the same waveform, a propagating target-pattern, but on sheets with different diameters of 1 cm (top) and 3 cm (bottom).

In our experiment, the gel produces a sharp oxidized green wavefront with a width $\approx 250 \mu\text{m}$ and a period of 450 seconds followed by a gradual return to the reduced (orange) state (Fig. 2A,B) propagating at a constant velocity of 30 $\mu\text{m/s}$ (Fig. 2B). The gel reacts to the chemical field with a periodic out-of-plane deformation with an amplitude of 1 mm (Fig. 2C). Note that propagating circular fronts can induce qualitatively different three-dimensional configurations, such as global buckling (Fig. 2D top) or symmetry breaking, wrinkle-like

evolving patterns (Fig. 2D bottom). As will be discussed below, the manifestation of a particular configuration is selected by the length scales of the system.

In order to obtain the relation between the BZ field and the reference metric, we compare the areal growth of each triangle on the sheet to its local BZ phase (i.e. color) over time (Fig. 3A). Since the ratio between the diameter and thickness of our disc is ≈ 20 (

Föppl–von Kármán number of 400) the measured area reflects reliably (better than $\pm 4\%$) the reference swelling (see Fig. S5). The measurements show that the two signals oscillate in synchrony with a phase shift. The areal-growth factor, $\Omega(\vec{r}, t)$, defined as the ratio of the measured area to the area in the reduced state, oscillates between 1 and 1.4. Cross-correlation between the BZ phase and swelling fields (see SI for the correlations analysis) shows that the deformation lags the BZ phase by $\tau \approx 55$ s (Fig. 3A). Such a delay is consistent with a gradual relaxation of the actual geometry to the reference geometry due to the time scale for fluid flow through the gel's pores. As shown in Fig. 3B, after incorporating this delay, we find a linear constitutive-relation between the phase and the growth.

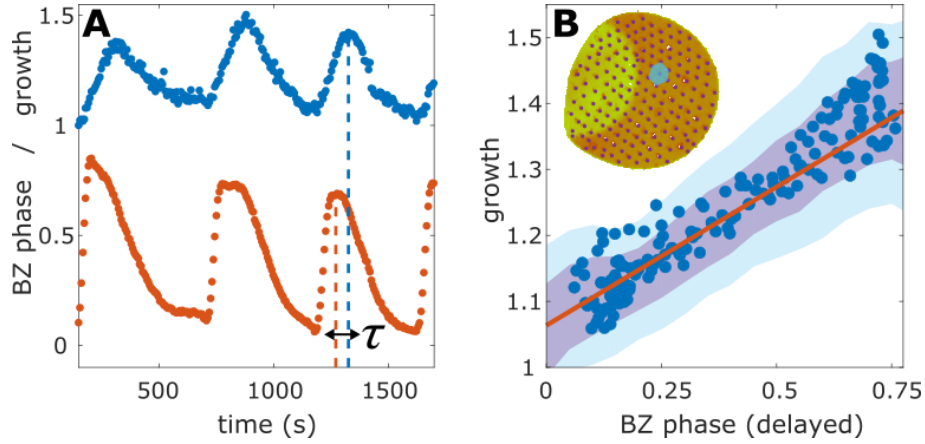


Fig. 3. Local chemo-mechanical activity: **(A)** Average BZ phase (red) and area growth (blue) measured from the single patch indicated in **(B)**. Both signals oscillate periodically, with a period of 450 seconds, and in synchrony with a time delay $\tau \approx 55$ s (see SI for the full analysis). The magnitude of the areal swelling is roughly 40%. **(B)** Growth as a function of the BZ phase delayed by 55 s (blue dots). These data collapse to a single curve indicating that the delay is uniform in time. The data from all patches is represented by the colored envelopes; 75% and 50% of all data falls within the blue and the purple envelopes, respectively. The red line is linear fit to the data from all patches. This fit is used below to model the dependence of the growth on the BZ phase. Note that the fit to all data agrees well with the data from a single patch. Inset: the patch (teal) on the triangular grid from which the local data in **(A)** and **(B)** were collected.

We use the theory of incompatible elastic sheets to connect the phase of the BZ field to the three-dimensional shape. The first step is a conversion of the varying phase field into an imposed reference metric and curvature field. For a locally isotropic deformation field (see Fig. S4), which is uniform across the thickness, the reference curvature vanishes ($\bar{\mathbf{b}} = 0$) and the resulting time-varying reference metric is always conformal to the flat metric:

$$\bar{\mathbf{a}}(\vec{r}, t) = \Omega(\vec{r}, t) \begin{pmatrix} 1 & 0 \\ 0 & 1 \end{pmatrix} \equiv \exp(\sigma(\vec{r}, t)) \begin{pmatrix} 1 & 0 \\ 0 & 1 \end{pmatrix} \quad 2$$

where σ is the logarithm of the areal swelling factor Ω . In this case, the reference Gaussian curvature is (see [34] page 297):

$$\bar{K}(\vec{r}, t) = -\frac{1}{2} \Delta_{\text{LB}} \sigma(\vec{r}, t) \quad 3$$

where $\Delta_{\text{LB}} \equiv \frac{1}{\sqrt{|\mathbf{a}|}} \partial_i \left(\sqrt{|\mathbf{a}|} \mathbf{a}^{ij} \partial_j \right) = \frac{1}{e^\sigma} (\partial_{uu} + \partial_{vv})$ is the Laplace-Beltrami operator (the curved-space Laplacian) for the reference metric (see SI). Eq. 3 is the key to understanding the conversion of the chemical BZ field into the evolving three-dimensional configuration: the reference Gaussian curvature at any point is determined by the Laplacian of $\sigma(\vec{r}, t)$, the logarithm of the swelling field, which is in turn determined by the phase of the reaction, modulo a time delay.

Having established the link between the BZ field and the imposed reference geometry, we next turn to an analysis of the non-Euclidean *elasticity* problem, i.e., finding the equilibrium configuration in 3D of a plate for a given reference metric [11]. Such problems have been extensively studied and it is known that the 3D configuration is set by a competition between stretching and bending. As in the case of constrained flat sheets [35], dimensionless groupings, such as the ratio of thickness to lateral extent, distinguish between bending or stretching dominated limits which yield qualitatively different configurations even for the same reference metric [16,36]. We observe in our system (Fig. 2D) the same rich set of configurations typical of NEPs. For example, the deformation caused by a circular BZ front can be highly localized on a small thick disc (Fig.2D bottom right, Movie S1) or more diffuse, generating a wrinkle-like deformation, in a large thin disc (Fig.2D bottom left, Movie S2).

We compute $\bar{K}(\vec{r}, t)$ from the BZ field using Eq. 3. These data exhibit the same periodicity of the BZ phase but a more complicated waveform. The BZ waveform switches sharply to an oxidized state on the leading front, and then gradually return to the reduced state in the tail (Fig. 2B). The asymmetry in the BZ phase manifest as a corresponding asymmetry in $\bar{K}(\vec{r}, t)$: small, negative, and slowly varying between fronts, and large and rapidly varying across negative and positive values within a narrow band around the leading front (Fig. 4A).

We also extract the actual Gaussian curvature, $K(\vec{r}, t)$, from the three-dimensional surface measurements, and compare these data with the reference curvature $\bar{K}(\vec{r}, t)$. Figure 4B shows that $K = \frac{1}{10} \bar{K}$ for small values of $|\bar{K}|$, but there is a cutoff value after which K no longer changes for large $|\bar{K}|$. Due to the asymmetry of \bar{K} , the deviation is most noticeable for positive values of \bar{K} . These data show that oscillations in the BZ field control the evolution of the three-dimensional configuration via Eq. 2 and Eq. 3, but not in a "purely-geometrical" way.

The cutoff in K reveals that our system is not in the "thin" limit where $K \approx \bar{K}$. The observed difference between the actual and reference curvatures results from the competition between stretching energy (minimal when there is no difference, as $\mathbf{a} = \bar{\mathbf{a}}$) and bending

energy (minimal at flat configurations, where $\mathbf{b} = 0$). The behavior of a NEP with a step or periodic reference metric was studied theoretically [32,37] and the dependence of K on the sheet thickness h and the front width δ is known. For the parameters of our system, these results (see Fig 3(b) in [32]) predict $\frac{\bar{K}}{K} \approx 10$, consistent with our measurements (see Fig. 4B Fig. 4 A). Moreover, a 2D finite element simulation of incompatible sheets yields the same result and additionally reproduces the observed cutoff with the same value for thickness equal to those of the experimental system (0.4-0.6mm). A more detailed numerical analysis appears in the SI.

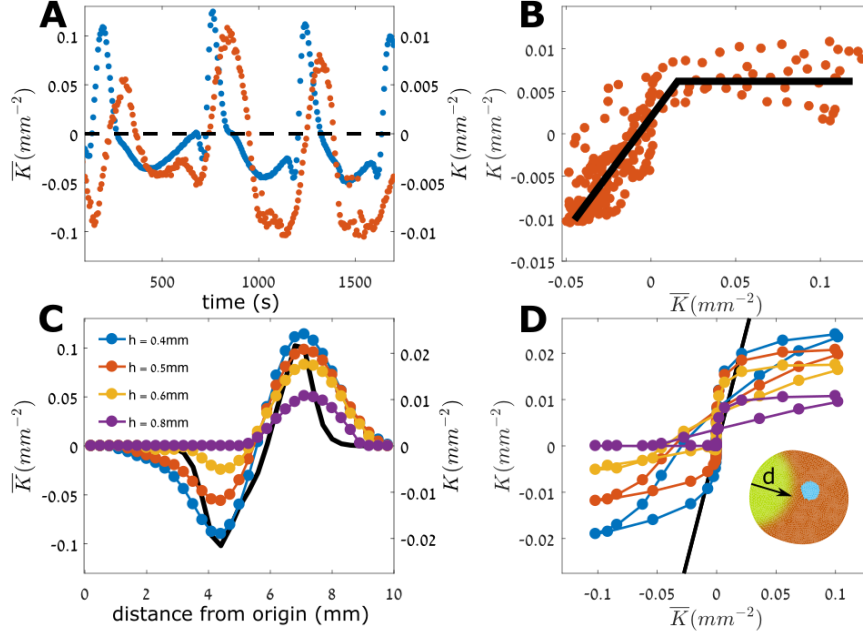


Fig. 4. Analysis of the Gaussian curvature: **(A)** The time-dependence of the reference (blue) and actual (red) Gaussian curvatures in a small patch. The large spikes in \bar{K} are due to the sharp changes in the reference metric. The oscillations in K display a much smaller amplitude. **(B)** Actual versus reference Gaussian curvature. These data show K follows \bar{K} for low values of $|\bar{K}|$ but saturates for $|\bar{K}| > 0.05 \text{ mm}^2$. **(C)** Reference curvature versus the distance from the origin of the propagating front, obtained from numerical simulations for different thicknesses. The reference Gaussian curvature (black) estimated over the patch highlighted in panel (D) is asymmetric and has a much larger amplitude than the actual curvature (color). These data suggest that the observed relationship in (B) is due to a competition between bending and stretching (see SI for more details). **(D)** Actual versus reference Gaussian curvature from simulations. The actual curvature displays a similar cutoff for thicknesses of around 0.6mm. Inset: the patch (teal) on the simulated triangular grid in which the local data in (C) and (D) were collected. The patch was chosen with correspondence to the patch on Fig 3 B.

This work provides the first realization of a synthetic autonomous multi-axial deformable sheet. The sheet “metabolizes” chemical energy to produce mechanical energy, i.e., periodic three-dimensional shape changes. Much of the underlying physics is well described by the theory of incompatible elastic sheets. This includes the conversion of the field characteristics of the BZ reaction into the relevant geometrical inputs (the reference metric), and the shape selection of the sheet, governed by a competition between stretching and bending. We note that other processes are likely to affect the evolving shape. Hydrodynamic effects, neglected here, are significant when the sheets are large and thin and when the evolution is fast. Additional dimensionless parameters are needed to include this effect and potentially will lead to even richer configuration space. We also neglected possible feedback of the

deformation on the propagation of BZ wave [38] that we expect to be significant in thinner sheets as well.

The concepts presented in this work - the autonomous conversion of planar deformations into curvature fields, the cutoffs in time and curvature - are general. They apply to many different systems, such as plates with non-flat background (non-oscillating) geometry [15,18] or the actuation of evolving spontaneous curvature due to gradients across the thickness, and are likely to apply to living cells [8,39] or be realized by different synthetic materials such as nematic elastomers [22,40]. In addition, we expect our results will stimulate new approaches to realizing autonomous soft machines.

References

- [1] M. Yoneda, Y. Kobayakawa, H. Y. Kubota, and M. Sakai, *Journal of Cell Science* **54**, 35 (1982).
- [2] U. Nath, B. C. W. Crawford, R. Carpenter, and E. Coen, *Science* **299**, 1404 (2003).
- [3] S. Armon, M. S. Bull, A. Aranda-Diaz, and M. Prakash, **115**, E10333 (2018).
- [4] G. M. Whitesides, **57**, 4258 (2018).
- [5] S. Maeda, Y. Hara, T. Sakai, R. Yoshida, and S. Hashimoto, **19**, 3480 (2007).
- [6] W. Hu, G. Z. Lum, M. Mastrangeli, and M. Sitti, *Nature* **554**, 81 (2018).
- [7] R. F. Shepherd, F. Ilievski, W. Choi, S. A. Morin, A. A. Stokes, A. D. Mazzeo, X. Chen, M. Wang, and G. M. Whitesides, **108**, 20400 (2011).
- [8] S.-J. Park *et al.*, **353**, 158 (2016).
- [9] M. Cianchetti, B. Mazzolai, L. Margheri, M. Follador, and P. Dario, *Advanced Robotics* **26**, 709 (2012).
- [10] K. Kondo, *Memoirs of the unifying study of the basic problems in engineering science by means of geometry* **1**, 5 (1955).
- [11] E. Efrati, E. Sharon, and R. Kupferman, *Journal of the Mechanics and Physics of Solids* **57**, 762 (2009).
- [12] E. Sharon, B. Roman, M. Marder, G. S. Shin, and H. L. Swinney, *Nature* **419**, 579 (2002).
- [13] B. Audoly and A. Boudaoud, *Physical Review Letters* **91**, 086105 (2003).
- [14] J. A. Gemmer and S. C. Venkataramani, *Physica D-Nonlinear Phenomena* **240**, 1536.
- [15] Y. Klein, E. Efrati, and E. Sharon, *Science* **315**, 1116 (2007).
- [16] S. Armon, E. Efrati, R. Kupferman, and E. Sharon, *Science* **333**, 1726 (2011).
- [17] Y. Klein, S. Venkataramani, and E. Sharon, *Physical Review Letters* **106**, 118303 (2011).
- [18] J. Kim, J. A. Hanna, M. Byun, C. D. Santangelo, and R. C. Hayward, *Science* **335**, 1201 (2012).
- [19] E. Sharon, B. Roman, and H. L. Swinney, *Physical Review E* **75** (2007).
- [20] M. Pezzulla, G. P. Smith, P. Nardinocchi, and D. P. Holmes, *Soft Matter* **12**, 4435 (2016).
- [21] Z. L. Wu, M. Moshe, J. Greener, H. Therien-Aubin, Z. H. Nie, E. Sharon, and E. Kumacheva, *Nature Communications* **4**, 7, 1586 (2013).
- [22] M. E. McConney, A. Martinez, V. P. Tondiglia, K. M. Lee, D. Langley, Smalyukh, II, and T. J. White, *Advanced Materials* **25**, 5880 (2013).
- [23] H. Aharoni, Y. Xia, X. Y. Zhang, R. D. Kamien, and S. Yang, *Proceedings of the National Academy of Sciences of the United States of America* **115**, 7206 (2018).
- [24] E. Siéfert, E. Reyssat, J. Bico, and B. J. N. m. Roman, **18**, 24 (2019).
- [25] E. Hajjesmaili and D. R. J. N. c. Clarke, **10**, 183 (2019).
- [26] M. Camacho-Lopez, H. Finkelmann, P. Palffy-Muhoray, and M. J. N. m. Shelley, **3**, 307 (2004).
- [27] R. Yoshida, T. Takahashi, T. Yamaguchi, and H. J. J. o. t. A. C. S. Ichijo, **118**, 5134 (1996).
- [28] S. Maeda, Y. Hara, R. Yoshida, and S. J. A. C. I. E. Hashimoto, **47**, 6690 (2008).
- [29] V. V. Yashin and A. C. J. S. Balazs, **314**, 798 (2006).
- [30] I. C. Chen, O. Kuksenok, V. V. Yashin, R. M. Moslin, A. C. Balazs, and K. J. J. S. M. Van Vliet, **7**, 3141 (2011).
- [31] P. Dayal, O. Kuksenok, and A. C. J. M. Balazs, **47**, 3231 (2014).
- [32] M. Moshe, E. Sharon, and R. Kupferman, *Nonlinearity* **26**, 3247 (2013).
- [33] R. Yoshida, M. Tanaka, S. Onodera, T. Yamaguchi, and E. Kokufuta, *The Journal of Physical Chemistry A* **104**, 7549 (2000).
- [34] B. O'Neill, *Elementary Differential Geometry* (Academic Press, New York, 1997), 2nd edn.
- [35] B. Davidovitch, R. D. Schroll, D. Vella, M. Adda-Bedia, and E. A. Cerda, *Proceedings of the National Academy of Sciences of the United States of America* **108**, 18227 (2011).

- [36] E. Efrati, E. Sharon, and R. Kupferman, Physical Review **E 80**, 016602 (2009).
- [37] J. Kim, J. A. Hanna, R. C. Hayward, and C. D. Santangelo, Soft Matter **8**, 2375 (2012).
- [38] P. W. Miller, N. Stoop, and J. J. P. r. I. Dunkel, **120**, 268001 (2018).
- [39] I. Nitsan, S. Drori, Y. E. Lewis, S. Cohen, and S. J. N. P. Tzlil, **12**, 472 (2016).
- [40] A. H. Gelebart, D. J. Mulder, M. Varga, A. Konya, G. Vantomme, E. Meijer, R. L. Selinger, and D. J. J. N. Broer, **546**, 632 (2017).

Supplementary Information for

Self-powered shape-transforming membranes: an active-matter approach to soft robotics

Ido Levin, Robert Deegan and Eran Sharon

Eran Sharon

email: erans@mail.huji.ac.il

This PDF file includes:

Supplementary text

Figs. S1 to S7

Captions for movies S1 to S3

Other supplementary materials for this manuscript include the following:

Movies S1 to S3

Supplementary Information

Methods

Gel preparation

Following Maeda et. al.(5), we dissolved **780mg** N-isopropylacrylamide (NIPA), **81mg** of ruthenium(II)tris-(2,2'-bipyridine)(Ru(bpy)₃²⁺) and **14mg** of N,N'-Methylenebis(acrylamide) (Bis-Acrylamide) in **2.5cc** of methanol and **0.5cc** of Dimethyl sulfoxide (DMSO). A second solution with **27.5mg** of 2-Acrylamido-2-methylpropane sulfonic acid (AMPS) dissolved in **2cc** of water was added to the mixture and purged in nitrogen for 10 minutes. **1cc** of a solution of 0.2M 2,2'-Azobis(2-methylpropionitrile) (AIBN) in toluene was added and mixed gently allowing the toluene separate and be removed.

The final solution was injected between two glass plates separated by a silicon-rubber gasket (Smooth-Sil 940) of the desired thickness. The glass plates were clamped together with a purpose-built vise and placed in an oven at 60°C for 20 hours. The polymerized gels were washed in ethanol for several days. Thereafter, the gel was placed in a series of ethanol-water baths of increasing water concentration (25%,50%,75%,100%) for a full day each. The fully washed gels were cut to the desired shapes with a laser-cutter and marked with a fine grid on the upper side of the gel by melting spots from a thin black plastic foil onto their surface with the laser. This grid defines a set of Lagrangian markers used in our geometrical analysis.

BZ solution

Dynamic measurements were done with the gel immersed in an aqueous solution of Nitric acid (HNO₃) **0.88M**, Sodium bromate (NaBrO₃) **0.084M** and malonic acid (C₃H₄O₄) **0.062M**. The solution was freshly prepared before each experiment and cooled to 20°C before introducing the gel.

Shape and BZ-field reconstruction

Gels were placed in a temperature-controlled cell filled with 10cc of the BZ solution. Two cameras were placed 30cm above the gel tilted at 14.5° with respect to each other. One camera was located vertically above the gel in order to minimize refraction. The gel was illuminated from below and was photographed with both cameras simultaneously every 5 seconds. A time-dependent 3D displacement field was extracted by matching corresponding markers between simultaneous images and tracking the markers through sequential image pairs. The evolution of the shape was calculated from the displacement field using a standard geometrical stereoscopy calculation corrected for the refractive index of the solution (Fig. S1).

Measurements of the changes in the area and the BZ-phase for a single triangle produced oscillating signals such as those shown in Fig. S2. The cross-correlation of these signals reveals a delay of around 60 seconds, whose exact value depends on the size of the gel. The phase of the BZ reaction extracted from the grayscale value of the green channel of the image along a line such as the one shown in Fig. S3.

Isotropy of local growth field

In order to calculate the reference Gaussian curvature, one must know the form of the reference metric, which depends on the local growth rule. A general local growth-field transforms circles into ellipses. Such a field is characterized by the areal growth, aspect-ratio and orientation of the ellipses. For BZ-gels the growth was assumed to be isotropic (i.e. circles are transformed into circles) since there is no obviously preferred direction.

To test the isotropy of the growth we examined the aspect-ratio of the triangles defined as

$$\text{AR} \equiv \frac{abc}{(a+b-c)(c+a-b)(b+c-a)} \text{ and compared this to the areal growth (using Heron's}$$

$$\text{formula for the area of each triangle: } A^2 = \frac{1}{4} (a+b+c)(a+b-c)(c+a-b)(b+c-a)).$$

The fluctuations of each property were defined to be the standard deviation of this value

$$\text{normalized it by its mean: } \delta a \equiv \frac{\sqrt{\text{var } \Delta a}}{\langle \Delta a \rangle}, \text{ where } \Delta a \text{ is its deviation from the initial state.}$$

A histogram of these values shows that while the fluctuations in the area are centered around 0.125, the fluctuations in the aspect ratio peak at 0 with an average of about 0.03 (Fig. S4). This result strongly supports our isotropic growth assumption.

Using the reference geometry to calculate spatial derivatives

In any formalism with both reference and actual geometries, the relevant geometry must be defined for each integration or differentiation. In our two-dimensional non-Euclidean models, the integration was defined with respect to the reference geometry (Eq. 1) since this is the geometry input to the model. However, this choice is only significant for higher orders in the thickness and therefore irrelevant for the bending and stretching terms. In this work, we treat the BZ dynamics as given and study the elastic response. However, a full model for this problem (incorporating the BZ-phase dynamics as well) may require a more elaborate definition of the spatial derivatives in the reaction-diffusion equation.

Numerical analysis

Our experimental results were compared with a non-Euclidean finite element simulation of an analogous problem: a disk with a radius of 5mm and various uniform thicknesses (0.4 to 0.6 mm) subject to a non-uniform growth of magnitude, Ω_0 , along a circular front with a typical width δ centered at varying distance d from the edge. Since the front width is of the same order-of-magnitude as the thickness, we used a fine grid of over 4000 faces. The specific functional form of the front is inconsequential and for simplicity was chosen to be

$$\Omega(\vec{r}) = 1 + \frac{\Omega_0}{2} \left[1 + \tanh \left(\frac{d - \|\vec{r} - \vec{r}_0\|}{\delta} \right) \right] \text{ where the parameters were chosen to agree with}$$

experiments ($\delta = 0.25\text{mm}$ and $\Omega_0 = 0.5$). By varying the distance of the front from its origin, we simulated the propagation of the BZ front: for each value of d we computed the

equilibrium configuration and the set of resulting configurations is analogous to the shape evolution. These simulations were used to estimate the deviations of the actual local area to the prescribed swelling field (Fig. S5). The small relative error (less than 4%) supports the results in Fig. 3B. Furthermore, the resulting shapes qualitatively match our experimental results for the relevant range of thicknesses (0.4-0.6) supporting the model as well (Fig. S6).

We also use these simulations to look for finite-thickness effects: by increasing the thickness of the gel, the sharp peaks in the Gaussian curvature spread and become more asymmetric due to the increasing cost of bending (Fig. S7) similarly to our experimental observations.

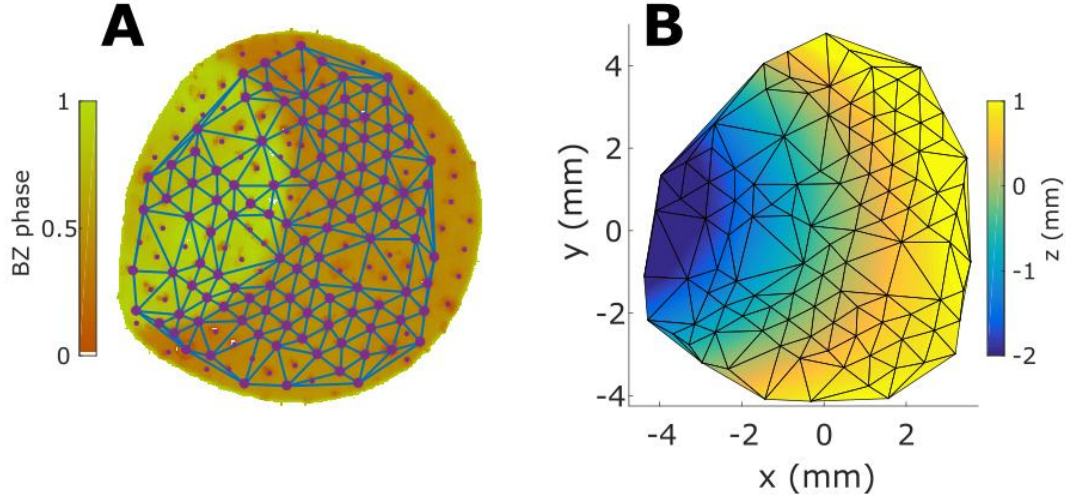


Fig. S1. Shape reconstruction: **(A)** The markers on the gels (purple dots) were tracked stereoscopically with two cameras over time. Markers that were successfully tracked by the algorithm over the entire measurement (larger dots) were used to produce a Lagrangian triangular lattice (blue lines) in three-dimensions. The BZ-phase in Lagrangian coordinates was measured at the center of each triangle. **(B)** Reconstruction of the gel's three-dimensional shape at $t = 0$ using the displacement of the Lagrangian markers between the two cameras. The gel was adhered by its left corner to the bottom of the cell ($z = -2$ mm) but was elsewhere free.

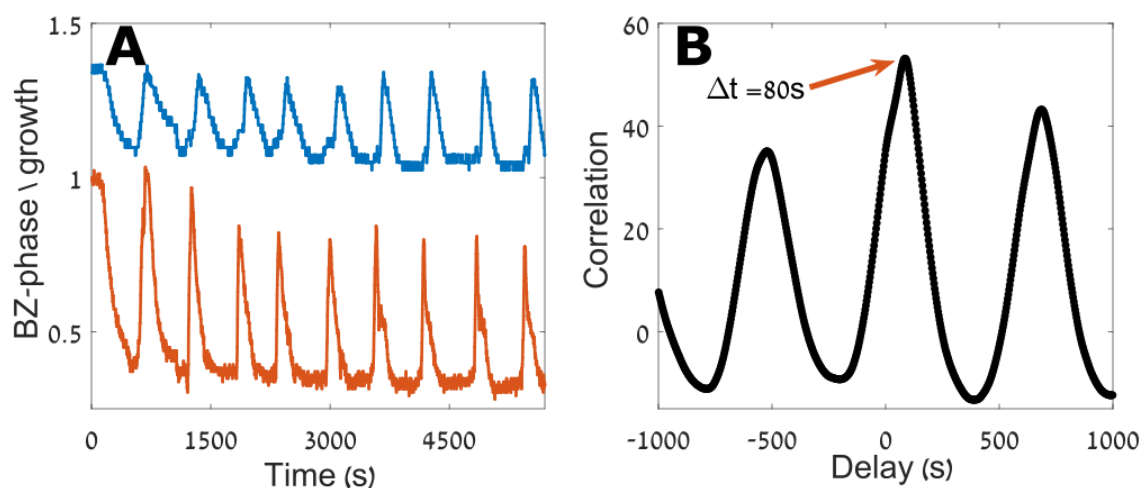


Fig. S2. Chemo-mechanical correlations: (A) The local BZ-phase and relative growth points over several oscillations. (B) Cross-correlating the signals in (A) reveals a strong correlation at a delay of 80 seconds in this particular sample which had a slower reaction rate with a period of almost 600 seconds.

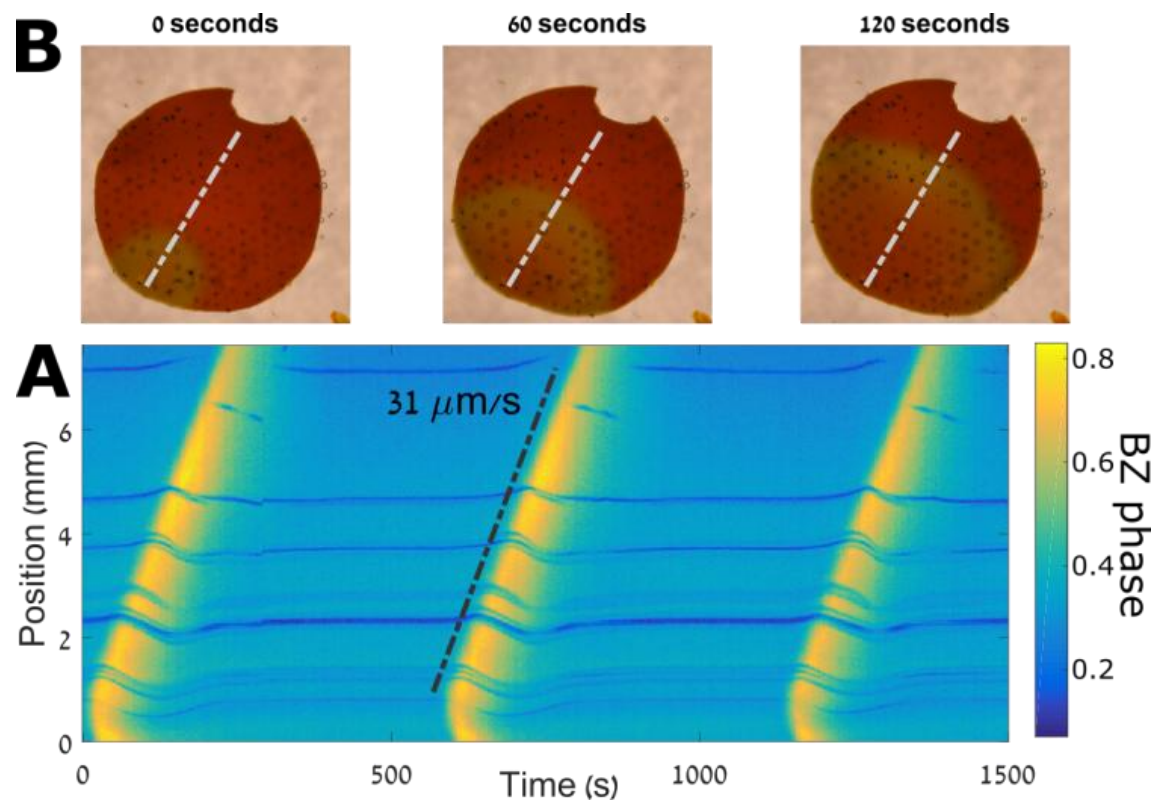


Fig. S3. Spatio-temporal map of BZ front propagation: (A) Three snapshots a front propagating along a BZ gel. The BZ field values were extracted along the marked line. (B) The time evolution of the BZ phase along that line.

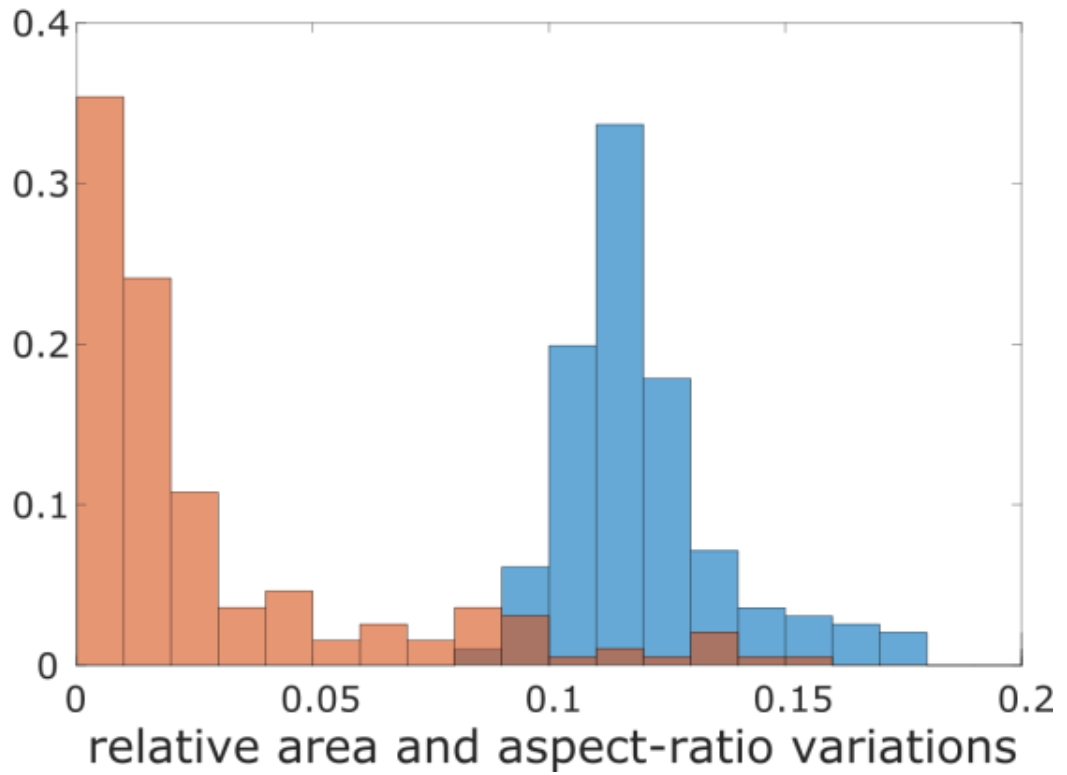


Fig. S4. Growth Isotropy: A histogram of the relative fluctuations, defined as the variance normalized by the mean, in the aspect-ratio (orange) and the area (blue) of each triangle. The tendency for small values of the aspect-ratio fluctuations (lower than 2%) are indicators of isotropic growth. Since the fluctuations are the standard deviation of the growth, their typical value (12%) is much smaller than the maximal growth-factor (40%).

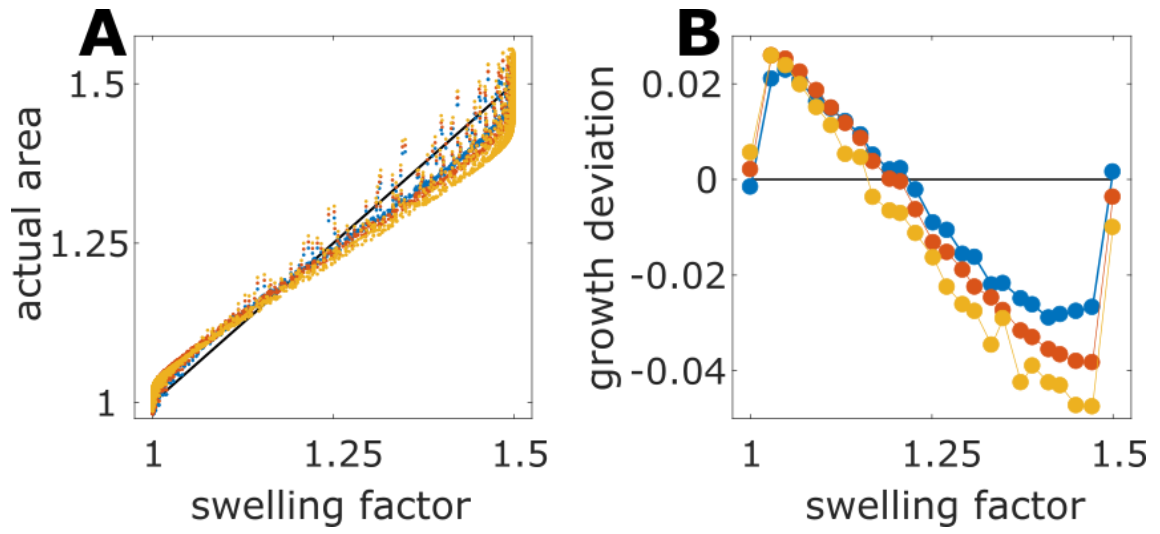


Fig. S5. Deviations of the actual area from the swelling field in our numerical results. **(A)** The actual area for three different thickness (0.4, 0.6 and 0.8 in blue, red and yellow, respectively) is very close to the prescribed swelling factor. **(B)** The deviation of the actual area from the prescribed area. As expected from elasticity, it increases with the thickness, it is negative in the swollen regions and positive in the shrunk regions. For the relevant thickness is smaller than 4%.

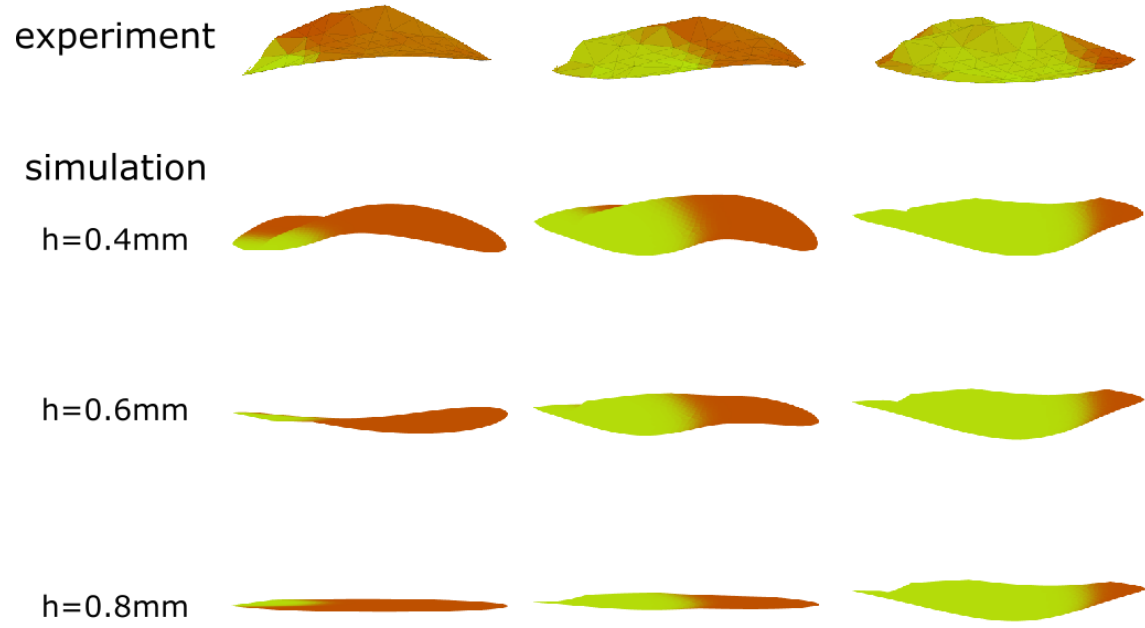


Fig. S6. Comparing experimental and numerical shape-evolution of a BZ gel disk. Top row: a sequence (left to right) of the measured shape (side view) during a single period. Row 2-4: The corresponding configurations calculated using finite-element simulation of different thicknesses (0.4, 0.6, 0.8 mm top to bottom). The spatial variation of the phase was selected to match the characteristics of the fronts observed in experiments (amplitude **50%**, width **250 μm** and diameter **10mm**). The experimental data resemble the numerical results for the thicknesses matching the experimental parameters (0.4 to 0.6).

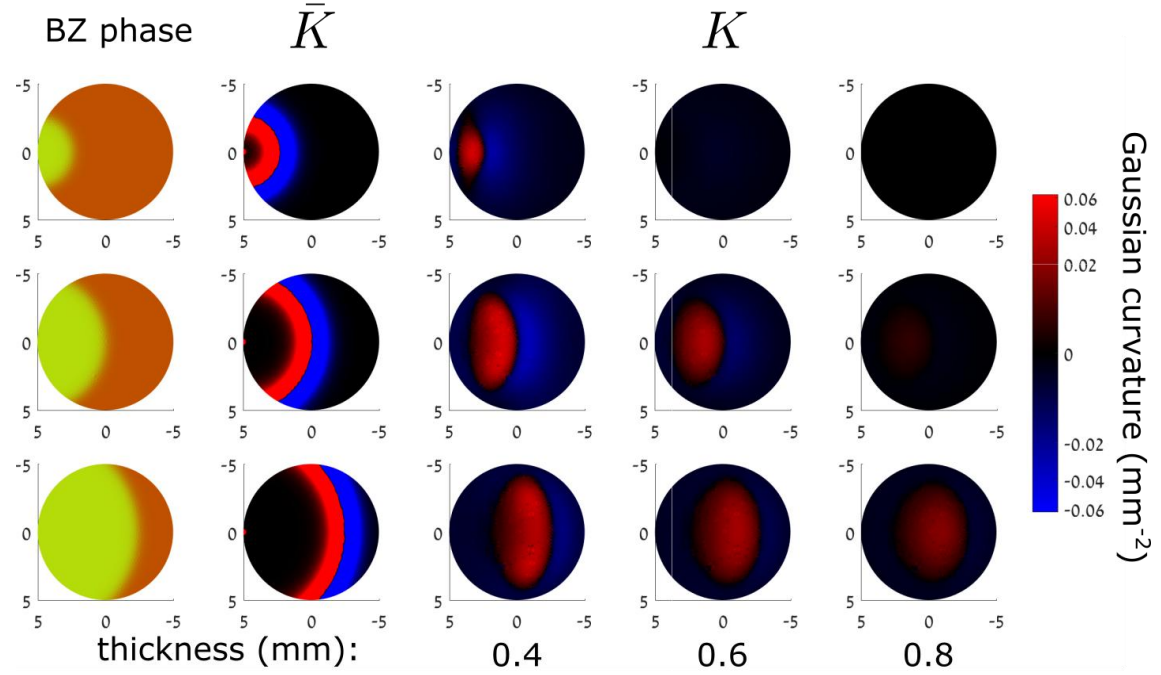


Fig. S7. Numerical evidence of finite-thickness effects. Column 1: simulated phase of the BZ reaction (top view) for different times (rows show an increasing time). Column 2: reference Gaussian curvature computed directly from the BZ field using Eq. 3. Column 3-5: actual Gaussian curvature for different thicknesses (values are indicated below the panels). The changes in the actual Gaussian curvature as the front propagates determines the evolution of the three-dimensional shape. Comparing the reference (column 2) and the actual Gaussian curvature of different thicknesses (0.4, 0.6, 0.8 mm left to right) demonstrates the effect of finite thickness: the magnitude of the actual Gaussian curvature is reduced and spread over a wider area. Note that the color is scaled nonlinearly in order to present the reference and actual values on the same scale.

Supplementary movies

Movie S1.

Several oscillations of a small BZ gel piece (diameter of 1cm, speed x250). A single target-pattern source at the edge of the gel generates a global change of shape.

Movie S2.

Several oscillations of the large BZ gel piece from Fig. 4D (diameter of 3cm, speed x250). A similar BZ pattern to MS1 now generates a wrinkled configuration due to the elastic shape-selection process.

Movie S3.

Evolution of the shape and the BZ phase of the small gel piece from Fig.2-4 (diameter of 1cm, speed x100). Two different projections of the reconstructed shape and BZ field demonstrate the significant change in curvature values.